INTERNATIONAL JOURNAL FOR NUMERICAL METHODS IN FLUIDS, VOL. 18, 361–383 (1994)

A COMPARISON OF SECOND-ORDER AND FOURTH-ORDER PRESSURE GRADIENT ALGORITHMS IN A σ-CO-ORDINATE OCEAN MODEL

JOHN D. McCALPIN

College of Marine Studies, University of Delaware, Newark, DE 19716-3501, U.S.A.

SUMMARY

In stratified three-dimensional models the use of a boundary-fitted vertical co-ordinate is known to produce errors in the horizontal pressure gradient calculation near steep topography. The error is due to the splitting of the horizontal pressure gradient term in each of the momentum equations into two parts and the subsequent incomplete cancellation of the truncation errors of those parts. In order to minimize these pressure gradient errors, a fourth-order-accurate pressure gradient calculation has been implemented and installed in SPEM, a three-dimensional primitive equation ocean model. The stability and accuracy of the new scheme are compared with those of the original second-order-accurate model in a series of calculations of unforced flow in the vicinity of an isolated seamount. The new scheme is shown to have much smaller pressure gradient errors over a wide range of parameter space as well as a greater parametric domain of numerical stability.

KEY WORDS Boundary-fitted co-ordinates Stratified flow Hydrostatic pressure

1. INTRODUCTION

The use of a transformed vertical co-ordinate which follows the terrain (here generically and imprecisely referred to as 'σ-co-ordinates') has long been a standard feature of atmospheric models. Its advantages are easy to see: it allows a direct specification of the bottom kinematic and stress boundary conditions; it allows the model to contain the correct bottom slope over topography; and it makes programming more convenient. The disadvantages of the scheme are somewhat more subtle but can be (perhaps artificially) divided into three categories: incorrect calculation of the pressure gradient forces near steep topography; diminished blocking of the flow due to steep topography; and decreased numerical stability. In this paper we address the first and third of these issues by implementing and testing a fourth-order-accurate algorithm for the calculation of the pressure gradient in SPEM, a three-dimensional primitive equation model.[1]

2. BACKGROUND

There are a variety of co-ordinate transformations available which map the vertical co-ordinate z into a constant range σ. Here we only deal with the simplest linear transformation:

$$\sigma = 1 + 2\frac{z}{h}, \tag{1}$$

CCC 0271–2091/94/040361–23

Received 13 January 1992
Revised 7 September 1993

where z is the vertical co-ordinate ranging from $z = 0$ at the fixed sea surface to $-h(x, y)$ at the sea floor. The transformed vertical co-ordinate ranges from $\sigma = 1$ at the sea surface to -1 at the sea floor. This particular transformation matches the desired range of the Chebyshev polynomials used for the vertical interpolation and differentiation in the model.

For this transformation the horizontal pressure gradient force is rewritten by use of the chain rule:

$$\nabla p|_z = \nabla p|_\sigma - \frac{1}{h} \nabla z|_\sigma \frac{\partial p}{\partial \sigma}, \tag{2}$$

where p is the pressure and ∇ is the horizontal gradient operator, calculated with respect to either constant z or constant σ, as specified. By use of the hydrostatic equation the second term may be rewritten, yielding a transformed pressure gradient of

$$\nabla p + g\rho\nabla z, \tag{3}$$

where g is the acceleration due to gravity, ρ is the (spatially varying) density of the fluid and the gradient operators are now implied to be with respect to constant σ.

We may divide the density field into three components: a large global mean ρ_0, a background stratification $\bar{\rho}(z)$ and a time- and space-dependent perturbation $\rho'(x, y, z, t)$. For oceanic applications the first term is typically three orders of magnitude larger than either of the latter two. The magnitudes of the two smaller terms depend on the strength of the oceanic flow regime being studied as well as the size of the domain under consideration, but they can be considered to be ordered ($\bar{\rho} \gg \rho'$) for nearly linear flow regimes and small domains or comparable for strong flow regimes or large domains.

Using this decomposition of the density field and again applying the hydrostatic relation, we may write the pressure as a sum of (i) an external part $p_0(x, y) = g\rho\eta \approx g\rho_0\eta$ from the deviation of the free sea surface $z = \eta$ away from the reference level $z = 0$ (plus any atmospheric pressure deviations in space), (ii) a mean part from the integral of ρ_0, (iii) another mean part from the integral of $\bar{\rho}(z)$ and (iv) a perturbation part from the integration of the perturbation density:

$$p(x, y, z, t) = p_0(x, y, t) + g\rho_0 z + g \int_0^z \bar{\rho}(z)\, dz' + g \int_0^z \rho'(x, y, z, t)\, dz'. \tag{4}$$

For oceanic applications the second term on the right-hand side is typically three orders of magnitude larger than the other three terms. Since this term contains no lateral derivatives (with respect to constant z), it does not contribute to the horizontal pressure gradient forces. Note, however, that this term *does* contribute to both components of the pressure gradient term in the transformed co-ordinate system. The contribution to the two components exactly cancels in the continuous case but does not in general cancel when finite difference approximations to the derivatives are employed. It is therefore imperative that this component of the pressure gradient be removed from the pressure before the derivatives are calculated,[2,3] since its truncation errors are also three orders of magnitude larger than the truncation errors of the dynamically active terms. The third term also has no horizontal derivatives and should also be removed before the pressure gradients are calculated. This will only help the overall accuracy of the scheme in regions for which the magnitude of $\bar{\rho}(z)$ is much greater than the magnitude of ρ', however.

Once the large mean pressure terms are removed, we wish to estimate the scale of the remaining pressure gradient error. A convenient case is that for which the perturbation density field is

independent of x and y and is characterized by an amplitude $\hat{\rho}$. As shown in Reference 4, a straightforward Taylor series expansion of a second-order finite difference scheme* reveals that the leading order truncation error terms of both parts of the transformed pressure gradient force, equation (3) (now divided by ρ_0 to give units of acceleration), scale like

$$\alpha \frac{g\hat{\rho}}{\rho_0}\left(\frac{\Delta x}{L}\right)^2 \frac{A}{L}, \tag{5}$$

where $\hat{\rho}$ is the characteristic amplitude of the density perturbations near the topography, L is the horizontal scale of the topography and A is the characteristic amplitude of the topography. The factor α is a scale factor that depends on the choice of the grid, the order of the model and the functional form of the topography. This error may be interpreted as a 'leaking' of the very strong gravitational/hydrostatic pressure gradient into the horizontal directions by way of the truncation errors.

The pressure gradient error is thus seen to scale as the product of the magnitudes of the density anomaly, the square of the grid resolution of the topography and the topographic slope. Assuming that the magnitude of the density anomaly is not under our control (once the large mean is removed), this leaves us with the options of smoothing the topography (thus increasing L and slightly decreasing A) or increasing the grid resolution. The former course is likely to be more effective at reducing the error, since the error dependence is at least cubic in L and only quadratic in Δx. Unfortunately, we are then solving a different problem from that with the original topography and the applicability of the model becomes suspect. The alternative course of decreasing Δx has the disadvantage of increasing the computational cost—both by increasing the number of grid points and by decreasing the maximum allowed time step.

An alternative approach to decreasing the pressure gradient error is to increase the order of the discretization and thereby change the functional dependence of the error scale. This approach is taken here, yielding an error which depends on the fourth power of the grid resolution of the topography. Obviously, this will only improve the situation if $\Delta x/L \ll 1$, but this is a requirement for accuracy with any scheme and so is not an additional requirement of the new model.

Note that many atmospheric models do not suffer from noticeable problems associated with pressure gradient errors in transformed co-ordinates. This is because most combine the use of smoothed topography with spectral representations in the horizontal and thus have exceedingly small truncation errors. On the negative side, this smoothing of the topography can cause diminished topographic blocking of the flow. A compromise system such as Mesinger's η-co-ordinate system[5] attempts to combine the best feature of z-co-ordinates and σ-co-ordinates but with an inevitable degree of subjectivity in the placement of the grid 'jumps'. To date, this diminished blocking of the flow has not proven to be a problem in oceanographic applications, since the flow is typically intensified at the sea surface where the co-ordinate system is most flat. The issue will not be further addressed here, though it will be of interest to researchers studying gravity currents and other bottom-trapped flows with σ-co-ordinate models.

The tendency of σ-co-ordinate models to display decreased numerical stability is poorly understood. One of the potential problems is the so-called 'hydrostatic inconsistency' which can arise if the grid slope exceeds a certain limit.[6] This problem is relatively easy to check for and to avoid. A discussion of stability limits for test configurations very similar to those of this paper

* This error estimate is obvious for the second term of equation (3) and is correct for the first term if vertical truncation errors are ignored. Since SPEM is spectrally accurate in the vertical, this assumption is reasonable unless the number of polynomials is very low.

is contained in Reference 7 (hereafter B&H). The results in this paper will be compared with the results of B&H wherever possible.

3. MODEL DESCRIPTION

The model used here is version 3.7 of the semispectral primitive equation model (SPEM), with the addition of the new fourth-order pressure gradient algorithm. The reader is referred to the original reference[1] for details concerning SPEM. In the horizontal directions the model uses second-order finite difference discretization on a staggered grid (the 'Arakawa C-grid') in an orthogonal curvilinear co-ordinate system. In the vertical direction the model uses a boundary-fitted co-ordinate which may or may not contain an additional analytic stretching. The discretization is by spectral collocation using Chebyshev polynomials, though the formal structure of the code is general enough to allow expansion in dynamical eigenfunctions as well.

The modification of the code employed in this study consisted of a small set of changes to the calculation of the pressure gradient forces. A standard four-point scheme was implemented which approximates the pressure gradient force using a fourth-order derivative operator for the derivatives and a fourth-order averaging operator for the density. For the staggered grid the fourth-order-accurate derivative operator is

$$\frac{\partial p}{\partial x_{i-1/2}} = \frac{-p_{i+1} + 27p_i - 27p_{i-1} + p_{i-2}}{24\Delta x} + O(\Delta x^4) \tag{6}$$

and the fourth-order-accurate averaging operator is

$$\bar{\rho}^x = \tfrac{1}{16}(-\rho_{i+1} + 9\rho_i + 9\rho_{i-1} - \rho_{i-2}) + O(\Delta x^4). \tag{7}$$

In all cases presented here the pressure gradient calculation for the row/column of velocity points nearest the boundary was excecuted using the original second-order-accurate algorithm. In the isolated seamount test cases used here this presents no problems, but difficulties could arise with more realistic topography. The finite difference equations for one-sided derivatives at fourth order employ a five-point asymmetric stencil. Careful tests will be required to determine if the use of these wider stencils actually increases the accuracy. These tests will be deferred to a later paper.

The reader should also note that only the terms responsible for the incomplete cancellation of the pressure gradient truncation errors are calculated with the fourth-order scheme. Several other spatial averages of metric terms arise owing to the transformation to orthogonal curvilinear co-ordinates. These are treated with the standard second-order-accurate schemes.

4. TEST CASES

The test cases employed here are all variants on the standard seamount test case of SPEM. The configuration is a channel closed on the north and south walls and recirculating through the east and west boundaries. The channel has a far-field depth of 5000 m and includes an isolated seamount in the centre. The height of the seamount is usually held fixed at 4500 m, but the lateral scale of the Gaussian-shaped seamount is varied between 6 and 50 km. Since the channel has dimensions of approximately 320 km × 320 km, the seamount is well isolated from the boundaries. The finite difference grid used in the horizontal directions is stretched, with finer resolution in the middle of the domain. The stretching is analytic, based on a cosine function,

resulting in a 2:1 variation in grid spacing from the centre of the domain to the edges. The stretching is applied in the same manner in both the x- and y-directions. The standard grid spacings range from 5·5 to 11 km. Some cases use a fine grid with twice the resolution.

All cases were performed with eight collection points in the vertical. Since no vertical viscosity or diffusivity is used in these cases, there are no viscous boundary layers in the vertical. Therefore this resolution is adequate to accurately resolve the vertical structure for all test cases presented here.

The background stratification for the experiments was exponential, with a 1000 m e-folding depth. Three different magnitudes were chosen for the density contrast: 'weak' at 0·5 kg m^{-3}, 'medium' at 2·0 kg m^{-3} and 'strong' at 4·0 kg m^{-3}. These correspond to temperature contrasts of 3·57, 14·28 and 28·57 K respectively.

For most cases the reference density field (a function of z only) was subtracted from the dynamic density field used by the model. The initial field for the model differed slightly from the reference field by

$$\rho_i = \bar{\rho}(z) + \hat{\rho} \exp(z/1000). \tag{8}$$

For the most commonly used value, $\hat{\rho} = 0{\cdot}2$ kg m^{-3}, the initial condition of the model was slightly less stably stratified than the reference field for each calculation. Note that because of this choice of initial condition, these cases have the same value of $\hat{\rho}$ in the scaling of the pressure gradient error, equation (5). The initial condition implies a perturbation density anomaly that is twice as large as that used in B&H, but it is still a rather weak anomaly, corresponding to a maximum temperature anomaly of less than 1·5 K at any z-level.

The standard time steps used were 128 steps/day (675 s) for the weakly stratified case, 256 steps/day (338 s) for the case of medium stratification and 512 steps/day (169 s) for the strongly stratified case. We calculated the first baroclinic mode phase speeds for the three cases by a second-order finite difference approximation of the vertical structure equation. This gives first baroclinic mode phase speeds of 1·35, 2·70 and 3·82 m s^{-1} for the weak, medium and strong stratification configurations respectively. The Courant numbers for the three cases are thus 0·182, 0·182 and 0·129 respectively.

Note that the direct calculation of the first baroclinic mode phase speed results in a different estimate of the Burger number than that used by B&H. They effectively estimate the first baroclinic mode phase speed as

$$c_p \approx N_0 H_0, \tag{9}$$

where H_0 is the far-field fluid thickness and N_0 is an estimate of the Brunt–Väissälä frequency using the formula

$$N_0^2 = g\Delta\rho/\rho_0 H_0. \tag{10}$$

This results in phase speed estimates of 4·89, 9·78 and 13·8 m s^{-1} respectively. Therefore their estimates of the Burger number are approximately 3·6 times the 'true' Burger number if that is intended to be defined as

$$S = R_d/L, \tag{11}$$

where L is the characteristic horizontal scale of the topography and R_d is the first internal radius of deformation defined as

$$R_d = c_p/f. \tag{12}$$

Here c_p is the phase speed of the first internal mode gravity waves and f is the Coriolis parameter.

A variety of other test configurations were used as well. These will be described in the sections containing their results. Owing to the very large number of calculations performed (about 200 runs), the results are expressed almost exclusively in terms of the maximum absolute value of the spurious velocity generated by the pressure gradient errors. For the sake of reference, two figures showing the spatial structure of the errors are presented in Figures 1 and 2. The first shows a typical contour plot of the barotropic streamfunction after 5 days of integration, while the second shows the three components of velocity through an x–z section at the same time. This is a 'bad' case, containing rather large errors, and is about half-way through the density adjustment phase of the adjustment process.

5. CONVERGENCE OF THE INITIAL PRESSURE GRADIENT ESTIMATE

An obvious first test of the model is to demonstrate the convergence of the second-order and fourth-order pressure gradient estimates for the initial conditions chosen. For a fixed grid and a varying seamount width the maximum value of the pressure gradient at $t = 0$ was calculated. We then calculate directly the magnitude of the velocity required to geostrophically balance the error, as suggested by Haney.[3] It will be shown in later sections that the actual adjustment process is more complex and involves a redistribution of the density field as well as the generation of geostrophic flows, but this measure of pressure gradient error has the advantage of being intuitively straightforward.

The results are shown in Figure 3 for both the second-order and fourth-order cases. On the basis of the scaling for the pressure gradient error, equation (5), we expect the errors to vanish as L^{-3} and L^{-5} respectively. The observed asymptotic orders for the schemes with the stretched grid are $-2{\cdot}53$ and $-4{\cdot}43$ respectively. These are approximately half an order slower than the

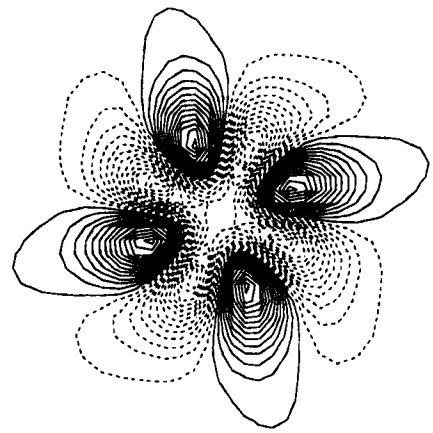

CONTOUR FROM -625000 TO 725000 BY 50000

Figure 1. Contour plot of the barotropic streamfunction of a typical unforced spin-up problem after 5 days. The spatial structure is essentially the same for the second-order and fourth-order results. The scale and structure of the topography can be seen in Figure 2

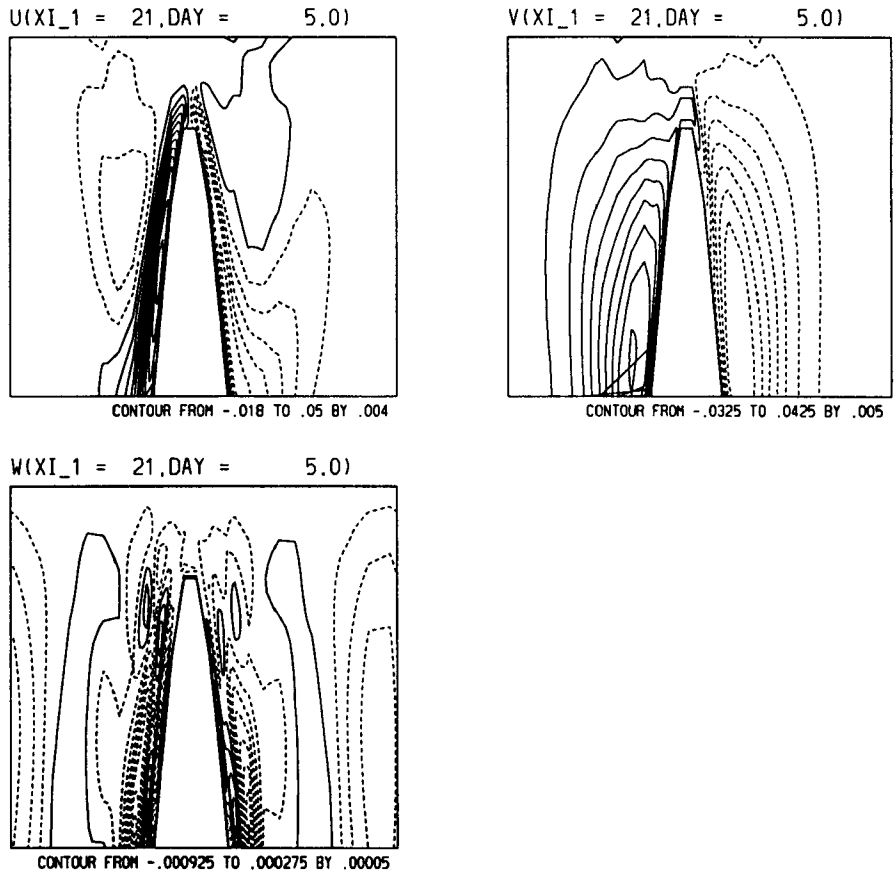

Figure 2. Contour of all three velocity components of an xz-plane at the same time as the streamfunction plot of Figure 1

desired result. The explanation comes from the fact that as the seamount width increases, the region of maximum slope moves away from the region of maximum grid resolution. Repeating the experiments with a uniform grid (with the same average spacing) shows the asymptotic convergence of order $-2{\cdot}94$ and $-4{\cdot}87$—almost exactly the desired values of -3 and -5. In these latter cases the errors were larger because the narrower seamounts were in a region of approximately 4 km resolution, compared with approximaely 2·75 km resolution with the stretched grid.

It is also possible to calculate the numerical parameter α from equation (5) using these results. Except for the narrowest cases (which are barely represented on the grid), the scale factor is approximately 1/6 for the second-order scheme and approximately unity for the fourth-order scheme. These values hold for both the uniform and non-uniform grids and vary by less than a factor of two across all the cases.

The representation of the pressure gradient error as an equivalent geostrophic velocity can be validated by running the model with linear dynamics and a fixed density field. Although this system is not very closely related dynamically to the full primitive equations, it has the desirable feature of allowing solutions which are steady geostrophic balances against the spurious pressure

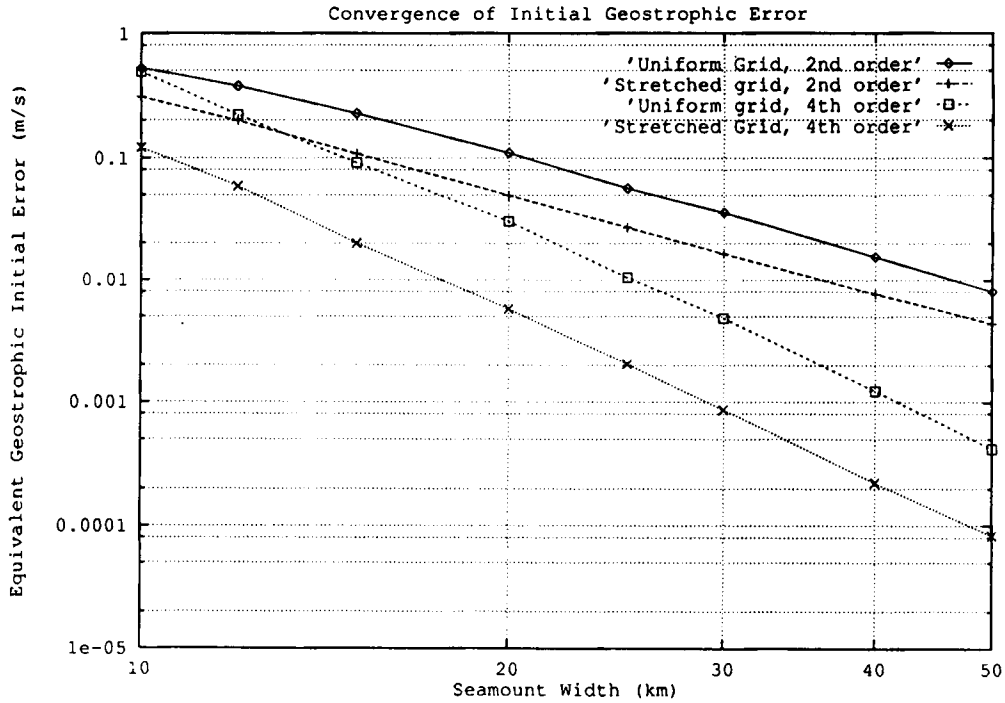

Figure 3. Maximum value of the geostropic velocity required to balance the initial pressure gradient error. Results are expressed as a function of seamount width and are presented for the second-order and fourth-order models for both uniform and stretched grids

gradient. Since the system is linear, it is sufficient to simply ignore the high-frequency inertial oscillations and observe the temporal mean of the solution.

The results of this case are presented in Figure 4. These results are for a very well-resolved case with a fairly strong density anomaly of 0·9 kg m^{-3}. The seamount amplitude is 4500 m, the lateral scale is 40 km and the grid spacing varies smoothly from 2·75 km at the centre of the domain to 5·5 km at the boundaries. The results for each case show the superimposition of inertial and geostrophic solutions of roughly equal amplitudes. The time-mean peak error velocity for the second-order case is roughly 40 times that of the fourth-order case.

For sufficiently small errors, it might be desirable to initialize the model using such a technique to develop an initially geostrophically balanced flow without disturbing the initial density field. This would eliminate the generation of undesired gravity wave energy from the solution when the full dynamics were turned on. Unfortunately, the gravity wave energy is not so easy to get rid of in a closed domain and the viscosity based on spatial derivatives is relatively inefficient at getting rid of gravity waves. A temporal damping could be added to effectively remove the gravity waves while leaving the steady geostrophic flow, but such a feature is not currently a part of SPEM.

Since the density field is fixed in this case, one would expect that the initial pressure gradient error determines the steady state part of the flow by geostrophy. This is the case. Comparing the mean of these time-dependent results with the estimates of the required balancing geostrophic

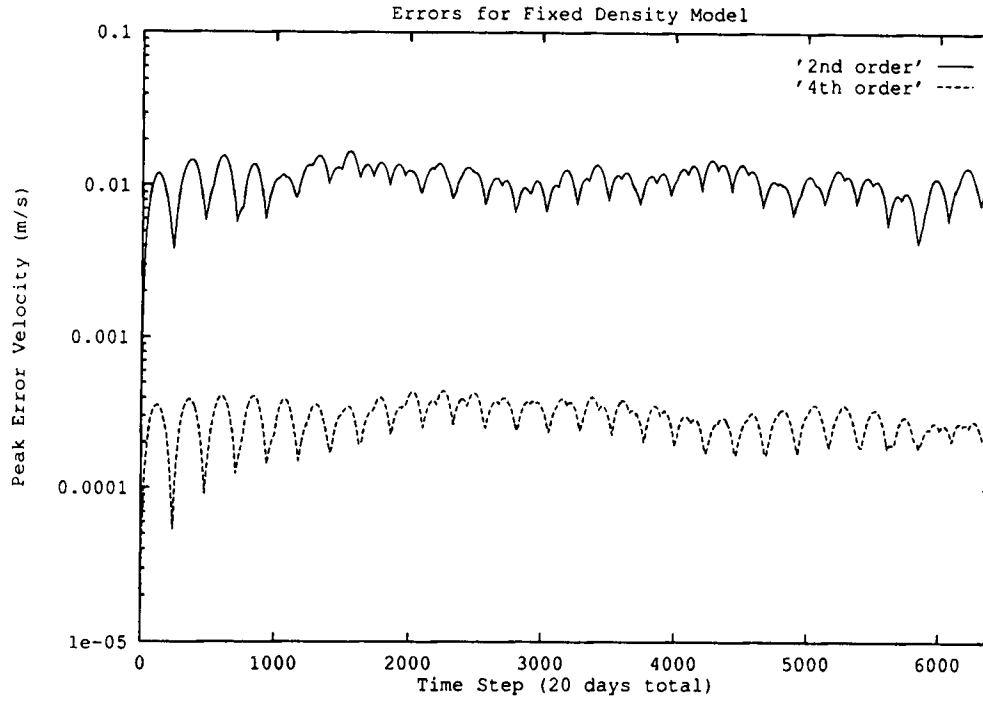

Figure 4. Peak error velocity from the fixed density model for a 5 day integration for the second-order and fourth-order models. The seamount amplitude is 4500 m, the lateral scale is 40 km and the initial density anomaly has magnitude 0·9 kg m^{-3}. The grid spacing varies from 2·75 km at the centre of the domain to 5·5 km at the boundaries. Note the logarithmic ordinate

velocity from Figure 3, we see that the second-order case had an estimate of 0·77 cm s^{-1} and an observed mean of 1·10 cm s^{-1}, while the fourth-order case had an estimate of 0·022 cm s^{-1} and an observed mean of 0·030 cm s^{-1}.

The differences in the estimates are due to the staggered grid. In the time-dependent case the Coriolis terms are averaged in x and y in the momentum equations, whereas in the steady state case the pressure gradient terms are averaged in x and y in the initial geostrophic balance. The averaging of the pressure gradient errors is also consistent with the direction of the error, which is a bias toward low estimates of the required geostrophically balancing velocity. Because of this bias, using this geostrophic balance as an initialization scheme would not provide perfect results. Nonetheless, it is expected that the initial gravity wave energy could be reduced by a significant factor by using such a balance. For the previous case it appears that the gravity wave amplitude reduction should be a factor in the range of three to four.

6. THE ROSSBY ADJUSTMENT PROCESS

If the convergence of the initial pressure gradient errors to zero could be related in a trivial way to the quasi-steady solution after the Rossby adjustment process, then the task of understanding the effects of the pressure gradient errors would be finished. Unfortunately, the actual behavior

of the model is far more complex, in part owing to the adjustment of the density field and in part owing to the model's requirement for non-negligible levels of lateral viscosity to maintain numerical stability.

At least four time scales are evident in this adjustment process. The first is an inertial scale, which for this model is $1/f = 10^4$ s. This is common to all Rossby adjustment models and it the only time scale present in the results of the fixed density model (see Figure 4). The second and third time scales are due to vertical then horizontal advection of the mean density field. These vary significantly depending on the size of the spurious velocities. They can be as short as $O(2)$ days but are more typically $O(10–20)$ days. The vertical advection comes from the fact that the solution exhibits significant cross-isobath velocities near the bottom which drive significant vertical velocities because of the bottom kinematic boundary condition (see Figure 2). This then causes lateral inhomogeneities in the density field which are advected horizontally. The fourth time scale is the dissipation scale due to lateral biharmonic viscosity. It is generally long, but for some of the narrow seamount cases it overlaps with the density advection time scales. Evidence of these time scales is present in Figures 6, 7 and others.

The combination of the several velocity growth time scales with the viscous decay and the uncertain stability of the model makes it very difficult to give quantitative estimates of what the 'final' adjusted geostrophic velocities would be in an otherwise equivalent inviscid system. We note that no matter how small the (finite) diffusion is, the only likely allowable steady solution is the trivial one.* Since the diffusion is typically not infinitesimal in the cases presented here (see Section 6.6), comparisons between runs must be somewhat qualitative.

The remainder of the paper will deal with the sensitivity and stability of the Rossby adjustment process of the full (non-linear) model. It is not the intent of this paper to detail the causes of instabilities within SPEM, but rather to show that the fourth-order pressure gradient algorithm significantly improves the model's stability (most likely by simply decreasing the magnitude of the noisy error field). Since virtually all numerical models have some sort of stability problems in the presence of strongly varying geometry, this result is likely to have general applicability even if the specific details of the implementation of the rest of the model change.

6.1 Dependence on seamount horizontal scale

Two series of test cases were performed with varying horizontal seamount scale—one with weak stratification ($R_d = 10{\cdot}5$ km) and the other with medium stratification ($R_d = 25{\cdot}7$ km). Seamount e-folding widths of 40, 20, 15, 12, 10, 8 and 6 km were used. All cases completed their 10 day runs without evidence of instability when using the standard time steps and standard levels of lateral biharmonic viscosity ('hyperviscosity') ($A_4 = 10^{10}$ m^4 s^{-1}).

A summary of the peak error velocity at day 10 for each of the cases is presented in Figure 5. The grid was held fixed across the runs and is the standard grid used for the SPEM seamount test cases. The grid spacing ranges from 5·5 km at the centre of the domain to 11 km at the boundaries. The figure makes it clear that the relative advantage of the fourth-order scheme is best for well-resolved topography. The fourth-order scheme is clearly much more accurate than the second-order scheme for seamount widths of 15 km or more, independently of the mean stratification.

The initial pressure gradient error for the fourth-order scheme is expected to decrease by a

* The other possible solutions with vanishing hyperviscosity that are consistent with the boundary conditions are streamfunction patterns varying as cubic polynomials in y. It is unlikely that one of these x-independent solutions will be found in a case with a seamount in the channel.

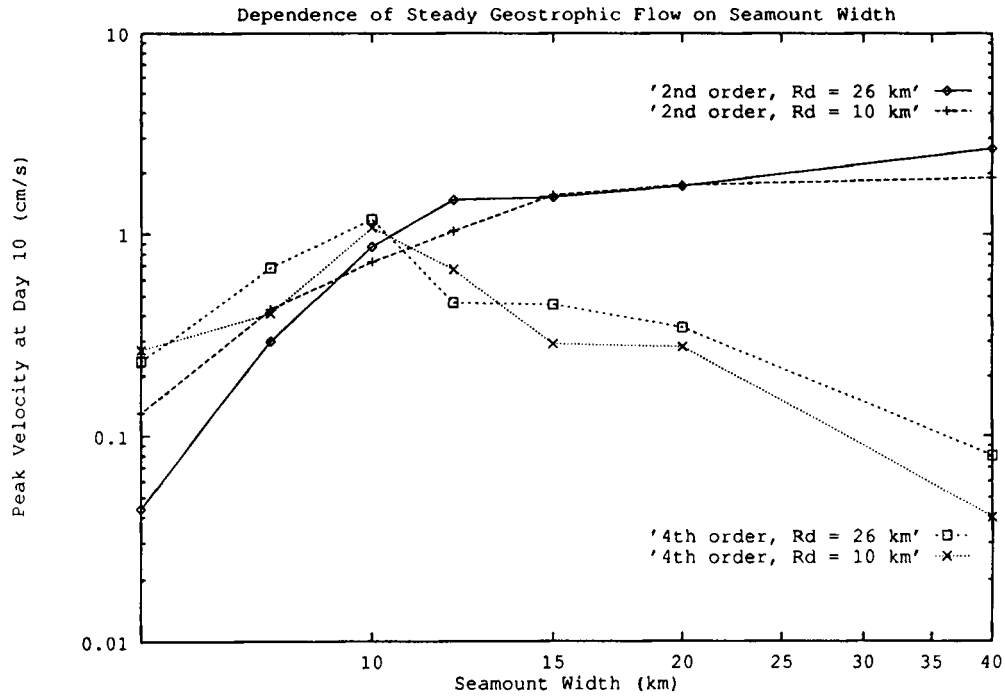

Figure 5. Peak error velocity at the end of a 10 day integration as a function of the seamount e-folding width

factor of $2^{4.5} = 22.6$ (see Section 5 for the reason) when the topographic scale doubles, while the initial pressure gradient error of the second-order scheme is expected to decrease by a factor of $2^{2.5} = 5.7$ when the topographic scale is doubled. The fact that the final velocities do not scale like the truncation error is an indication of the fact that a more complex adjustment process is taking place.

Careful examination of Figure 5 shows that the peak velocity at day 10 is increasing approximately as $L^{0.5}$ for the second-order model. This is rather distressing, since the pressure gradient force which drives the error is decreasing as $L^{-2.5}$. This implies that the adjustment process is amplifying the peak velocity by a factor proportional to L^3. The results of the fourth-order model are decreasing as $L^{-1.5}$, also implying an adjustment transfer function of order L^3.

These results are inconsistent with the theory of inviscid Rossby adjustment (see e.g. Reference 8). The simplest model of linear, inviscid Rossby adjustment assumes a homogeneous fluid and that the vertically integrated potential vorticity $q = (v_x - u_y + f)/h$ is conserved. By requiring that the final state be geostrophic, one can solve the linear one-dimensional problem for sinusoidal initial conditions. The solution specifies that the transfer function for peak velocity should be of the form

$$V_{\max} \propto \frac{1}{L} \frac{1}{1/L^2 + 1/R_d^2}, \tag{13}$$

where L is the horizontal scale of the pressure field and R_d is the Rossby radius of deformation appropriate to the vertical structure of the pressure anomaly. This function is asymptotically

proportional to L for small L and to $1/L$ for large L, with a maximum at $L = R_d$. The maximum slope of order L^1 is not strong enough to account for the results observed with the model. In any event, the function $V_{max}(L)$ is almost constant when L and R_d are of the same order as is the case here. Therefore we cannot expect the linear inviscid Rossby adjustment process to explain these results.*

The fact that the error increases with L can also not be explained by assuming that some of the cases were not yet 'spun up'. This is because the *narrower* seamount cases adjust more rapidly (because the initial errors and slopes are larger, implying larger vertical advection and thus faster adjustment—compare Figures 6 and 7), so that if any cases are displaying anomalously low values, it is the well-resolved ones—quite the opposite of what we need to explain the observed transfer function.

The observed error growth of the model must therefore be due to effects not contained in the linear, inviscid Rossby adjustment model. These effects include advection of density, viscosity and numerical energy non-conservation.

The role of advection of density is crucial in the spin-up problem, but other than controlling the times scales (which we have just noted acts in the wrong sense to explain the L^3 transfer function), it is not evident that this can act to control the peak velocity in the way that is observed.

The lateral coefficient of biharmonic viscosity was kept fixed across these runs. Since the scale of the solution matches the scale of the topography, the viscous terms decrease across the series as L^4. Thus for a fixed integration time the dependence on L can be expected to range from L^4 (where viscosity is an $O(1)$ term) to L^0 (where viscosity is negligible). The apparent dependence of order L^3 shown here would be consistent with a level of viscosity that is important over most of the parameter range tested. The scaling of the viscous terms relative to the Coriolis terms is still small. For example, for the $L = 10$ km case,

$$\frac{A_4}{fL^4} = \frac{10^{10}}{10^{-4}(10^4)^2} = 10^{-2}. \tag{14}$$

However, the viscous time scale for this case is

$$L^4/A_4 = 10^6 \text{ s} \tag{15}$$

or about 11 days. This would account for a decay by a factor of three over a 10 day integration and is probably a large part of the explanation of the behaviour for the shorter scales ($L < 20$ km). However, for $L = 20$ km this time scale is 176 days, so the decay at 10 days is only 5% and can be neglected. Since the viscosity can be neglected for the 20 and 40 km cases, it clearly cannot be called on to account for the difference in the transfer function for these larger scales.

Energy non-conservation was not tested explicitly. It is expected to be at the level of the truncation error and therefore proportional to Δx^2, but its dependence on L is unknown.

Whatever their exact causes, the seriousness of these combined errors depends on a combination of the user's accuracy requirements and the available grid resolution. Note that the increase in maximum velocity with L is especially important in applications for which the integrated mass transport is of interest, since the error velocity is both larger and extending over a larger region. The fourth-order scheme provides a reduction in the error which is more than sufficient

* A more complicated Rossby adjustment model (obtained by including the spatial dependence of R_d caused by the finite amplitude topography) shows an even weaker dependence on L. In this case topographic vortex stretching dominates the solution, making the transfer function for peak velocity a monotonically decreasing function of L The stratified model is expected to display behaviour somewhere between these two extremes.

to overcome the increased tendency of the model to incorrectly generate flow at larger scales and also more than sufficient to decrease the total error transport as the scale increases.

6.2 Dependence on mean stratification

SPEM is set up in such a way that a 'mean' stratification is removed from the dynamic density variable. This mean stratification is a function of z only and is typically chosen to minimize the absolute magnitude of the dynamic density variable, since it is that magnitude which feeds the spurious pressure gradient force. For the unforced experiments executed here, it is clearly unreasonable to set the initial density field equal to the mean stratification. This would result in a vanishing dynamic density field which would produce zero pressure gradients to round-off error. B&H chose an initial condition

$$\rho_i = \bar{\rho}(z) - 0{\cdot}1 \exp(z/1000), \tag{16}$$

which corresponds to a temperature anomaly of only 0·5 K at 400 m (near the top of the seamount). At the location of the maximum slope of the co-ordinate system the density anomaly is considerably smaller. This temperature anomaly is much smaller than those which could reasonably be expected to exist due to geostrophic flows and therefore makes their tests too 'easy' for the model. In the cases presented here with the medium and strong stratifications, temperature anomalies an order of magnitude stronger than this might be expected at mid-thermocline depths.

Despite these reservations, a series of experiments were run that closely parallel those of B&H. The time series of peak velocity for the case of a 40 km wide seamount are presented in Figure 6 and those for the case of a 20 km wide seamount are presented in Figure 7. The most immediately striking results are that (i) the fourth-order model has much lower errors than the second-order model and (ii) the error velocities are only weakly dependent on the mean stratification. This is perhaps not surprising, since it is the perturbation density rather than the mean density which goes into the scaling of the spurious pressure force in equation (5).

6.3 Dependence on perturbation density magnitude

As mentioned in the previous subsections, the size of the initial density anomaly is expected to have a large impact on the magnitude of the spurious current generated in the initial adjustment process. Therefore a series of experiments were conducted using much larger initial density anomalies. This was implemented by simply modifying the mean density field (which is subtracted from the dynamic density field) to be a constant of 28·0 kg m^{-3}. Note that a *global* mean density of 1000 kg m^{-3} is subtracted from all cases, since it does not contribute to any dynamics. The same initial temperature profiles were used as in the previous cases, so the initial density anomalies were 0·3, 1·8 and 3·8 kg m^{-3} times the exponential vertical decay function. These fields correspond to surface temperature anomalies of 2·14, 12·86 and 27·14 K respectively. While the last two of these are perhaps larger than one should encounter at any z-level if a suitable reference field is chosen, they do give insight to the behaviour of the model when strong density anomalies are present.*

The tests with large initial density anomalies were run for seamount widths of 40, 20 and 15 km. The results are presented in Figures 8–10 respectively. These results again shown the

* In an earlier model[4], the author only subtracted a global mean density from the dynamic density field. The results of this subsection show clearly why that model failed to perform adequately in the simultaneous presence of strong topography and strong stratification.

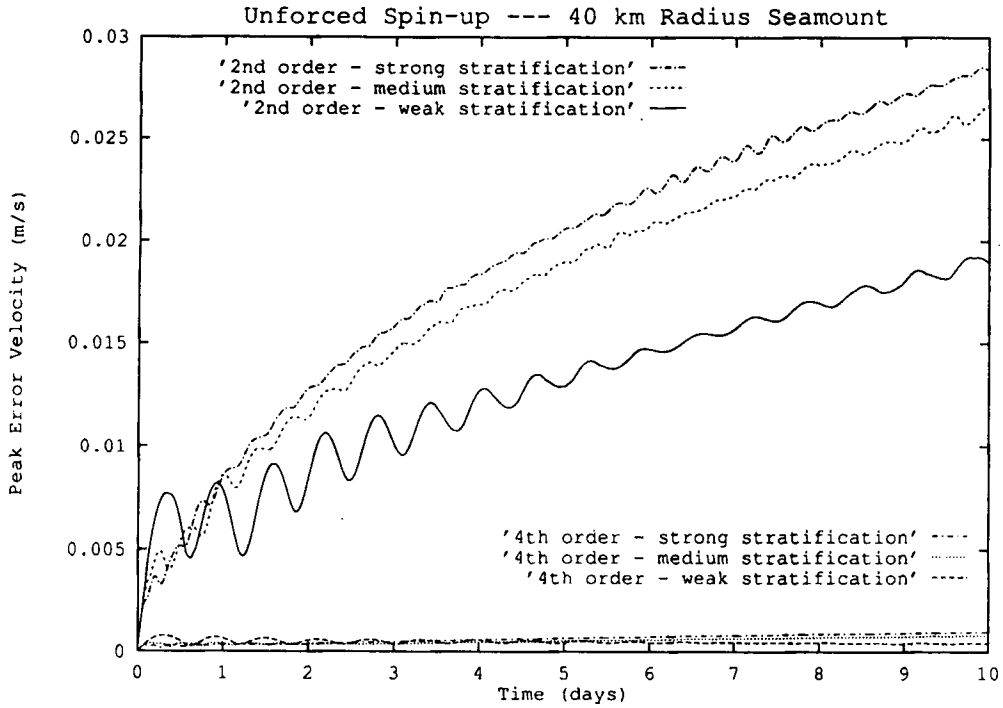

Figure 6. Time series of peak velocities for unforced 'spin-up'cases over a 40 km wide seamount in the presence of three levels of stratificatin. The upper curves are from the second-order model while the lower curves are from the fourth-order model

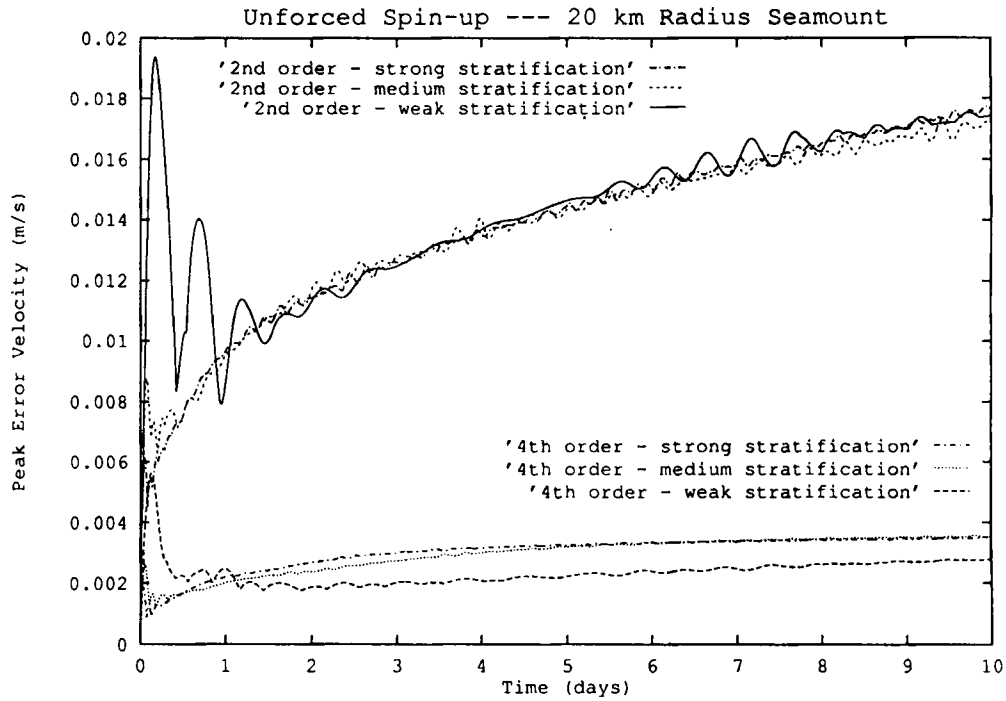

Figure 7. Time series of peak velocities for unforced 'spin-up' cases over a 20 km wide seamount in the presence of three levels of stratification. The upper curves are from the second-order model while the lower curves are from the fourth-order model

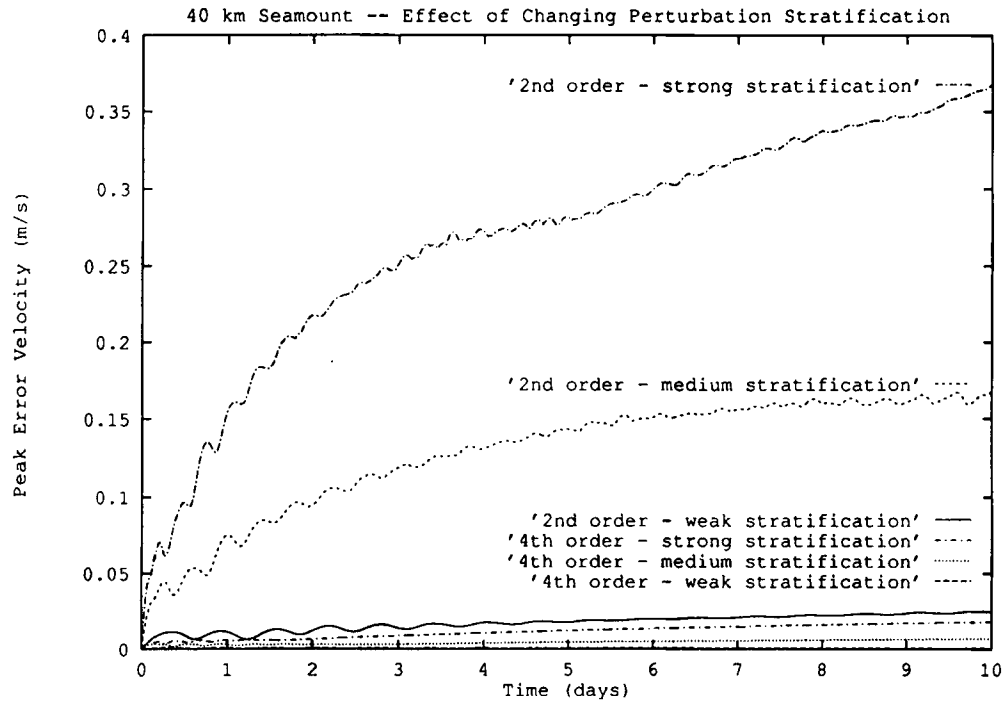

Figure 8. Time series of peak error velocities for a 40 km seamount in the presence of large initial density anomalies. In each case only a global reference density was subtracted from the initial field rather than a z-dependent 'mean' stratification

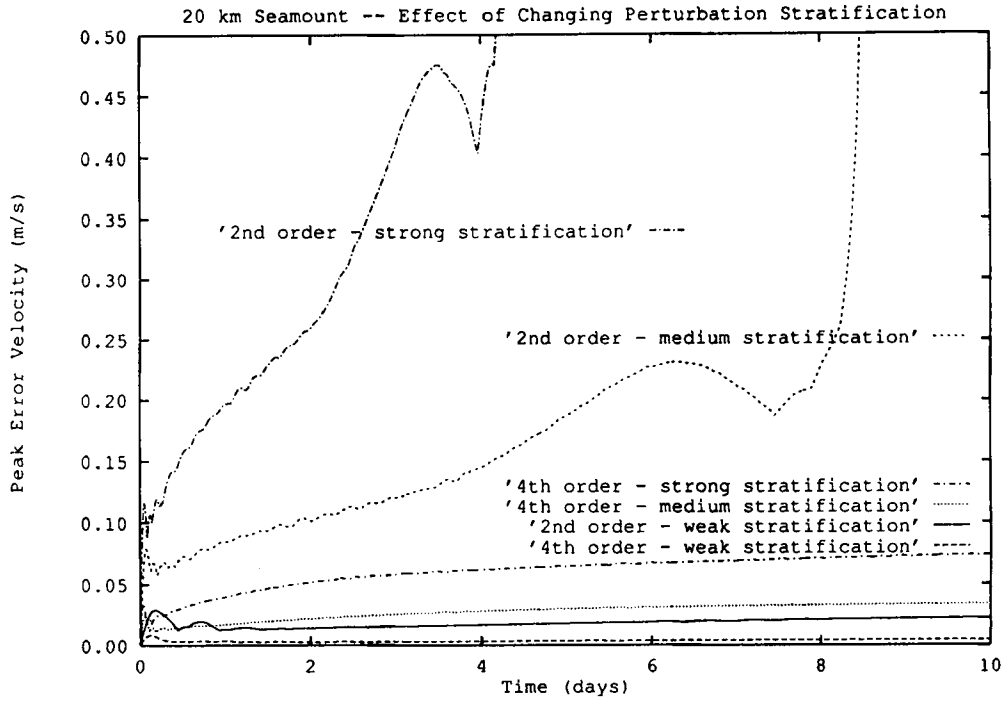

Figure 9. As Figure 8 but for a 20 km wide seamount

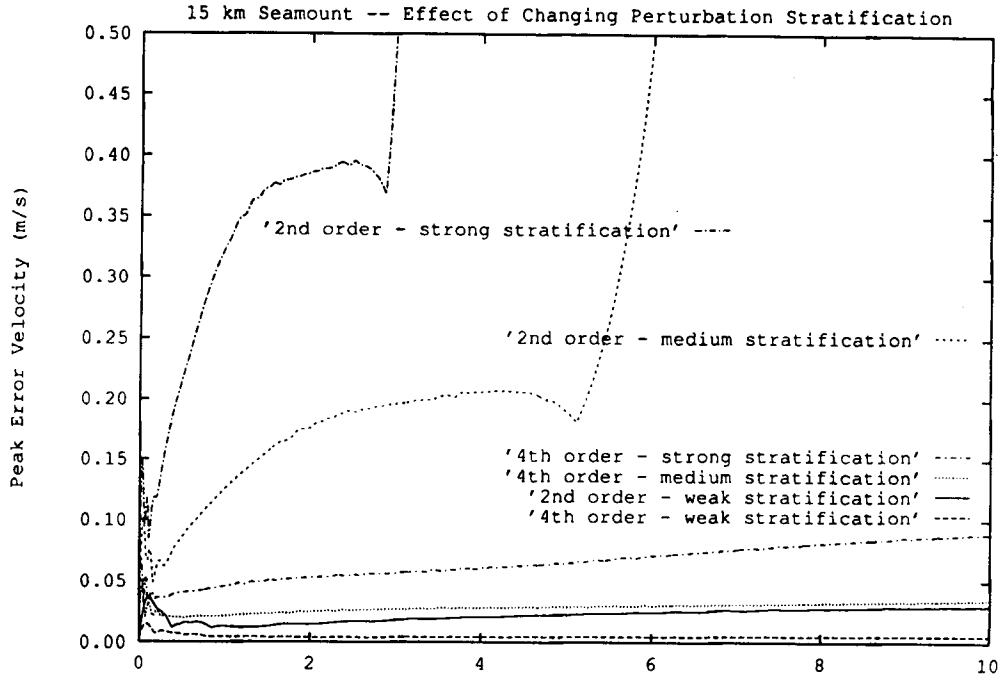

Figure 10. As Figure 8 but for a 15 km wide seamount

marked superiority of the fourth-order scheme. In addition, the results show restrictions on the stability of the second-order scheme that are relaxed with the fourth-order algorithm. The second-order scheme was unstable in four of nine cases—whenever the seamount widths was less than or equal to 20 km and the stratification was simultaneously stronger than the weakest case. The fourth-order scheme was stable for all cases, though the error velocities reached 9 cm s^{-1} in the worst case.

6.4 Dependence on time step

The results showed essentially no dependence of the error magnitudes or error evolution on the time step. This is consistent with the usual expectation that the restrictions on stability are more stringent than the restrictions on accuracy.

The fourth-order schemes are expected to have a somewhat more stringent stability limit on the time step.[9] This was only observed in two sets of test cases.

One, with $L = 40$ km, was stable with the second-order model with medium stratification and a Courant number of 0·364, while the fourth-order model was unstable in the same configuration. Both models were stable when the Courant number was reduced to 0·182. Both models were *unstable* for a Courant number of 0·364 when the seamount scale was reduced to 20 km. In addition, the strong stratification tests were rerun with a Courant number of 0·258 and were stable for both second-order and fourth-order differencing for both the 40 and 20 km seamount width cases.

The second case was for $\hat{\rho} = 0{\cdot}9$ and a 20 km seamount. The second-order model was stable

with a Courant number of 0·174, but the fourth-order model required a slightly lower Courant number—it was stable at a Courant number of 0·138.

The difference between the two cases discussed above is that the first had a relatively weak dynamic density anomaly of 0·2 kg m^{-3}, while the second was part of the series with stronger anomalies, in this case 0·9 kg m^{-3}. It is not surprising that the significantly stronger noise in the latter case made the calculation slightly less computationally stable.

6.5 Dependence on seamount height

A series of experiments were run with an intermediate level of stratification (6·43 K or 0·9 kg m^{-3}), a constant 'mean' stratification and a variety of seamount heights. Seamount amplitude of 100, 200, 500, 1000, 1500, 2000, 2500, 3000, 3500, 4000 and 4500 m were used.

The results show an approximately exponential increase in the maximum error velocity at day 10 as a function of seamount height. This is to be expected because of the exponential increase in perturbation density with height. Figure 11 shows the results for both the second-order and fourth-order models. The approximately exponential dependence on seamount height is suggested in Figure 12, which presents the same data with the ordinate on a logarithmic scale.

6.6 Dependence on lateral viscosity

All the model experiments described in this study were performed with no lateral diffusion of density. This approach is suggested by the fact that diffusion of density along sigma surfaces (which is the easiest formulation to implement) generates horizontal pressure gradients wherever the sigma surfaces are not flat. This then produces horizontal pressure gradients which

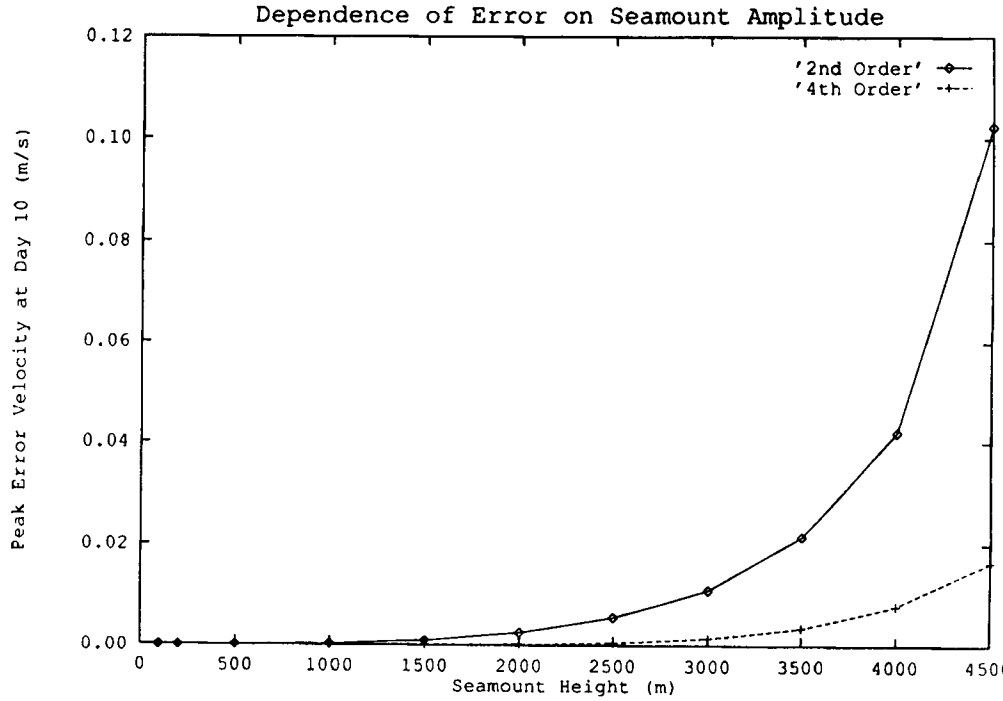

Figure 11. Dependence of peak error velocity at day 10 on the height of the seamount above the 5000 m abyssal plain

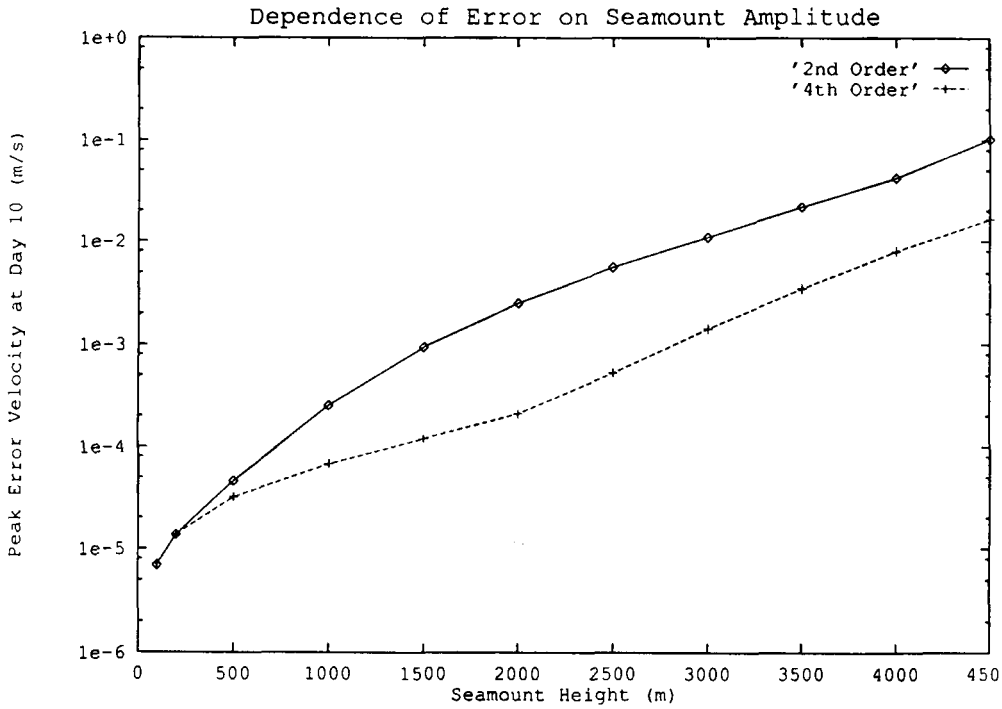

Figure 12. Figure 11 but using a logarithmic scale for the ordinate. The dependence is approximately exponential

drive geostrophic currents in much the same way as the pressure gradient errors being addressed in this study.

Unfortunately, the absence of horizontal diffusion of density means that any short-scale information that is generated in the pressure field (by topographic scale advection of density) will remain there and continue to force short scales in the momentum equations (which are proportional to the gradient of the pressure). Finite difference models are rather sensitive to the existence of such short-scale information in the velocity fields and their stability properties are significantly compromised by its continuous introduction. Because of this continuous forcing at short scales, some lateral viscosity is required in the momentum equations to maintain stability. This 'lateral' viscosity is actually calculated on sigma surfaces but does not directly cause difficulties in the same way that iso-sigma diffusion of density does. A constant coefficient biharmonic formulation is used for the lateral viscosity here.

It is the nature of viscosity to be more active at short scales. Therefore one would expect that in those cases where viscosity is needed to retain stability, the dynamical balance would include viscosity as a non-negligible term. This has been observed to be the case for poorly resolved topography. An example was a case with $L = 20$ km and the standard grid (5·5 km resolution). The geostrophic velocities at any pont in time were strongly dependent on the lateral viscosity. The dependence was less than linear, suggesting that for the low-frequency part of the solution the dynamical balance included three terms: Coriolis force, pressure gradient and lateral viscosity. This behaviour was true for both the second-order and fourth-order models, though the absolute errors were much smaller and the amount of viscosity required to maintain stability was somewhat smaller with the fourth-order code.

Because of the feedback mechanism described above, the model requires non-negligible levels of lateral viscosity even with well-resolved topography. The levels are not large in the non-dimensional sense but do influence the peak error velocity by factors of up to three as the viscosity is varied from the minimum level required for stability to the maximum level allowed by linear stability (i.e. we keep the time step determined by the CFL condition on the hyperbolic part of the problem). For a seamount width $L = 40$ km and the fine resolution grid (2·75 km minimum spacing) the peak error velocity at 10 days was 0·8 mm s^{-1} with $A_4 = 10^9$ m^4 s^{-1}, increasing to 2·3 mm s^{-1} with $A_4 = 10^8$ m^4 s^{-1}.

Care was taken in all the other cases in this study to present only results computed with the same level of lateral viscosity. This is the reason why no standard convergence tests were performed—it was not possible to run a sequence of experiments covering a large range of grid spacings with the same lateral viscous coefficient. Either the coarse resolution cases were unstable or the fine resolution cases required unreasonably short time steps for stability. Convergence testing by keeping the grid fixed and varying L was therefore used instead.

7. DISCUSSION

It is of interest to attempt to find the 'correct' set of parameters which control the accuracy and stability of the σ-co-ordinate model. For the case of fixed $\hat{\rho}$, B&H express their results in terms

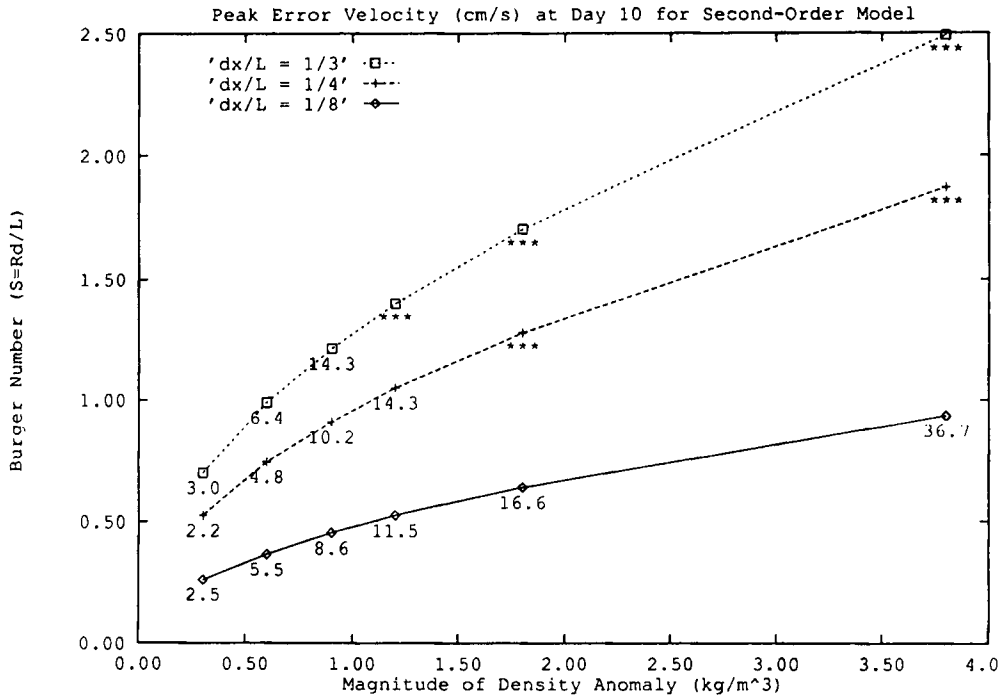

Figure 13. Dependence of peak error velocity at day 10 on the Burger number and density anomaly magnitude for the second-order model. The lines connecting the data points indicate contours of constant $\Delta x/L$. Unstable runs are marked by asterisks

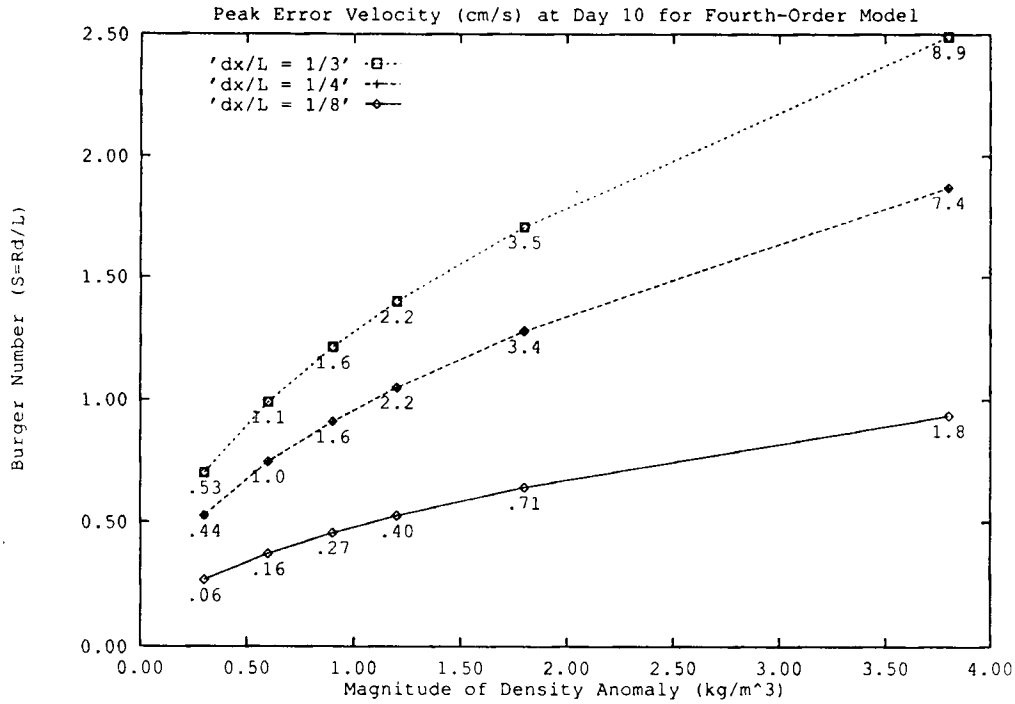

Figure 14. Dependence of peak error velocity at day 10 on the Burger number and density anomaly magnitude for the fourth-order model. The lines connecting the data points indicate contours of constant $\Delta x/L$

of the Burger number S and the maximum value of a non-dimensional ratio of grid steepness to local depth:

$$r \equiv \frac{h_+ - h_-}{h_+ + h_-}, \tag{17}$$

where h_+ and h_- refer to the depths of the fluid on either side of the test point. The parameter r_{max} is defined as the largest value of r occurring in the domain. Their results show that both the stability and accuracy are rather weak functions of S. This is likely a direct result of choosing a fixed perturbation density for all experiments.

An alternative parameteric representation is to study the stability and accuracy as functions of the Burger number S and $\hat{\rho}$. Note that for the fixed grid used in these experiments, S implicitly contains both the non-dimensional scale of the topography (R_d/L) and the grid resolution ($\Delta x/L$). Figure 13 gives the final (day 10) peak error velocities as a function of Burger number S and density anomaly magnitude $\hat{\rho}$ for the second-order model. Five of the experiments were unstable and are marked with asterisks. The same information for the fourth-order model is presented in Figure 14. For this algorithm all cases were stable, but the two cases with $\hat{\rho} = 3{\cdot}8$ combined with Burger numbers of 1·87 and 2·49 displayed rather large error velocities. Comparison of the two figures shows a rather broad range in which the errors of the fourth-order scheme are reduced by factors of 10–20 relative to the second-order scheme. In the 'easy' limit of small density perturbation and small Burger number the ratio increases to about 40:1.

8. CONCLUSIONS

The use of a fourth-order-accurate pressure gradient algorithm has been shown to drastically reduce the spurious velocities generated near steep topography in a stratified, three-dimensional ocean model employing a vertical boundary-fitted co-ordinate. For the seamount test case here the error was reduced by a factor of 10–20 over most of the parameter space.

The details of the adjustment process of a model initialized with a 'flat' density field have been shown to be considerably more complex than one would expect based on a simple Rossby adjustment model. In addition to the generation of inertia–gravity waves, the model experiences significant evolution associated with advection of the density field vertically then horizontally by the spuriously generated currents. Because of this added complexity, the final 'spun-up' velocities of the full three-dimensional model are not trivially related to the initial pressure gradient amplitude error.

For fixed Burger number the stability and accuracy and clearly dependent on the magnitude of the perturbation density $\hat{\rho}$ as well as on the grid resolution. Although no obvious combination of controlling parameters has been found which clearly delineates the behaviour of the model, the new fourth-order scheme has been shown to provide the model with a greater parametric domain (in terms of Burger number, topographic slope and perturbation density) of both accuracy and stability than did the second-order scheme. The approximately 200 numerical experiments performed in this study showed no cases for which the second-order scheme could be considered either more accurate or more cost-effective.

ACKNOWLEDGEMENTS

This work was supported by a grant from the Ocean Science Division of the National Science Foundation, OCE-09206176. Some of the computations were made possible by a grant of computer time from the National Center for Atmospheric Research. The National Center for Atmospheric Research is administered by the University Corporation for Atmospheric Research with funding from the National Science Foundation.

APPENDIX I: COMMENTS ON COMPACT DIFFERENCING SCHEMES

In many instances the compact differencing schemes are capable of producing results superior to the standard wide stencil schemes.[10] Compact differencing schemes work by estimating the leading term of the truncation error by a finite difference approximation on the solution. This produces an implicit system which for first derivatives on an unstaggered grid looks like

$$\frac{1}{6}\frac{\partial p}{\partial x_{i+1}} + \frac{2}{3}\frac{\partial p}{\partial x_i} + \frac{1}{6}\frac{\partial p}{\partial x_{i-1}} = \frac{p_{i+1} + p_{i-1}}{2\Delta x} + \frac{\Delta x^4}{180}\frac{\partial^5 p}{\partial x_i^5}. \tag{18}$$

On a staggered grid one must define the derivatives at the midpoints of the intervals separating the p-points. The scheme is otherwise analogous.

Unfortunately, the tridiagonal system implied in equation (18) requires knowledge of the derivative of p at both boundaries. Such information is not directly accessible from the governing equations or kinematic boundary conditions.

A very good approximation to the normal derivative of p at the boundaries can be obtained by reducing and scaling the normal momentum equation. For the case of a boundary at constant

x the momentum equation reduces to

$$-fv = -\frac{1}{\rho_0}\frac{\partial p}{\partial x} + A_h \frac{\partial^2 u}{\partial x^2}, \tag{19}$$

where A_h is the coefficient of Laplacian eddy viscosity.

For cases with slip boundary conditions v does not vanish and the momentum equation may be geostrophic, depending on the scaling of the viscous terms. The viscous terms will be at their largest when the normal velocity increases most rapidly away from the wall, as at the separation point of a western boundary current. Assuming that the normal velocity increases from zero to $O(1)\,\mathrm{m\,s^{-1}}$ in one baroclinic radius of deformation and that the eddy viscosity coefficient is $O(10^3)$, we estimate a scale of

$$\frac{(1)(1000)}{50000^2} = 4 \times 10^{-7} \tag{20}$$

for this force. This can be compared with the force caused by geostrophic flow tangential to the boundary, fv. The ratio indicates that the largest possible derivative that can be caused by the viscous terms in the normal momentum equation is equivalent to that caused by a tangential geostrophic flow of

$$\frac{4 \times 10^{-7}}{f} = 4 \times 10^{-3}\ \mathrm{m\,s^{-1}} \tag{21}$$

and can thus be considered to be negligible. The size of the viscous term is even smaller when biharmonic viscosity is applied with typical coefficients:

$$\frac{(1)(10^{10})}{50000^4} = 1{\cdot}6 \times 10^{-9}. \tag{22}$$

For the case of no-slip boundaries the Cariolis term vanishes and the pressure gradient must balance the force from the viscous terms. Although this value may be non-zero, it is from the above arguments $O(10^{-3})$ relative to interior pressure gradients and thus may be approximated as vanishing.

If the preceding arguments are accepted, then the normal derivative of pressure may in all cases by assumed to be exactly geostrophic at the boundary. The difficulty with the C-grid used in SPEM is that the discrete version of the geostrophic relationship that must be used to obtain the normal derivative of pressure at a normal velocity point is

$$-f\bar{\bar{v}}^{xy} = -\frac{1}{\rho_0}\frac{\partial p}{\partial x}, \tag{23}$$

where the overbars indicate a spatial averaging. In order to obtain fourth-order accuracy, one must employ fourth-order-accurate averaging operators here in both directions. This requires a 4×4 array of v-points and would be quite expensive, as well as of dubious accuracy. Note that the tridiagonal system directly couples the entire domain, so second-order errors introduced at the boundary are propagated throughout the domain at each time step. This is not the case with the wide stencil scheme.

APPENDIX II: THE ARAKAWA B-GRID

Many large-scale ocean circulation models employ a different staggered grid, the Arakawa B-grid, for which both components of the velocity are evaluated at the same points. The staggering of the pressure points requires that the pressure gradient terms be averaged in y for

the u-momentum equation and in x for the v-momentum equation. In order to achieve formal fourth-order accuracy with this grid, a fourth-order averaging operator would be required. Note, however, that this average is in the direction orthogonal to the direction of the pressure derivative and therefore does not contribute directly to the component of the pressure gradient error which causes the trouble.

More specifically, if one calculates the fourth-order-accurate derivatives first, one receives the benefit of the fourth-order-accurate cancellation of the truncation errors of the two components of the pressure gradient error. If one then performs second-order-accurate averages of the results, this will decrease the overall accuracy of the scheme but cannot undo the cancellation of the pressure gradient errors that the fourth-order scheme provided.

The formulae for fourth-order-accurate derivatives and averages are the same on the B-grid as on the C-grid, since they are all being evaluated at the midpoints of intervals.

REFERENCES

1. D. B. Haidvogel, J. L. Wilkin and R. Young, 'A semi-spectral primitive equation ocean circulation model using vertical sigma and orthogonal curvilinear coordinates,' *J. Comput. Phys.* **94**, 151–185 (1991).
2. M. Batteen, 'On the use of sigma coordinates in large-scale for ocean circulation models,' *Ocean Modell. Newslett.*, April (1988).
3. R. Haney, 'On the pressure gradient force over steep topography in sigma coordinate ocean models,' *J. Phys. Oceanogr.*, **20**, 610–619 (1991).
4. J. D. McCalpin, 'The design and implementation of a three-dimensional primitive equation ocean circulation model,' *Ph.D. Thesis*, Florida State University, 1990.
5. F. Mesinger, 'A blocking technique for representation of mountains in atmospheric models,' *Riv. Meteorol. Aernonaut.*, **44**, 195–202 (1984).
6. F. Mesinger, 'On the convergence and error problems of the calculation of the pressure gradient force in sigma coordinate models,' *Geophys. Astrophys. Fluid Dyn.*, **19**, 105–117 (1982).
7. A. Beckman and D. B. Haidvogel, 'Numerical simulation of flow around a tall isolated seamount. Part I: Problem formulation and model accuracy,' *J. Phys. Oceanogr.*, **23**, 1736–1753 (1993).
8. A. E. Gill, *International Geophysics Series*, Vol. 30, *Atmosphere–Ocean Dynamics*, Academic, New York, 1982.
9. G. Haltiner and R. T. Williams, *Numerical Prediction and Dynamic Meteorology*, Wiley, New York, 1979.
10. H.-R. Chang and H. N. Shirer, 'Compact spatial differencing techniques in numerical modeling,' *Mon. Weather Rev.*, **113**, 409–423 (1985).